

Phase transition and optimal actuation of active bilayer structures

Yin Liu^{a,b}, Yunteng Cao^c, Xi-Qiao Feng^d, Changyong Cao^{a,e,*}

^a Laboratory for Soft Machines & Electronics, School of Packaging, Michigan State University, East Lansing, MI 48824, USA

^b School of Civil Engineering, Wuhan University, Wuhan, Hubei 430072, China

^c Department of Civil and Environmental Engineering, Massachusetts Institute of Technology, Cambridge, MA 02139, USA

^d Institute of Biomechanics and Medical Engineering, AML, Department of Engineering Mechanics, Tsinghua University, Beijing 100084, China

^e Departments of Mechanical Engineering, Electrical and Computer Engineering, Michigan State University, East Lansing, MI 48824, USA

ARTICLE INFO

Article history:

Received 25 February 2019

Received in revised form 6 April 2019

Accepted 12 April 2019

Available online 20 April 2019

Keywords:

Snap-through instability

Bistability

Soft active materials

Bilayer

Phase diagram

ABSTRACT

Active bilayer structures have great potential applications in the fields of drug delivery, soft robots and actuators. In this paper, we have investigated the phase transition and optimal actuation of bilayer structures under biaxial active strains. A theoretical model is developed to predict the bending curvature of the bilayer in the large deformation regime, instead of the traditional Timoshenko's buckling solution. A Riks path-following procedure in the finite element method is utilized to trace the active-strain induced snap-through instability to identify the phase boundaries of bistability in the bilayer. The phase transition diagram from bistability to monostability and the general requisites to generate a snap-through instability by varying active strains are thoroughly discussed based on the bending curvature and energy landscape from simulations. Using the average curvature to characterize the actuation efficiency, we find that the anisotropy of active strains can be utilized to tune the bending angle and configuration of bilayer structures. The presented model and the obtained phase diagram provide a potential guidance for future design of high-performance bilayer-based actuators and machines in a broad range of applications.

© 2019 Elsevier Ltd. All rights reserved.

1. Introduction

Active bilayer structures hold promise for important applications in the fields of drug delivery, soft robotics, sensors and actuators [1–6]. In an active bilayer, two layers with distinct stimuli-responsive expansion or shrinkage properties are bonded together to form a composite shell structure. A bilayer can bend due to the mismatch strains induced by the expansion or shrinkage of the active layers, leading to various functions in both natural and synthetic systems [7–13]. For example, the scales of pine cones, consisting of two distinct layers with different angles of microfibrils in cells, can open and close in response to the change of humidity to spread seeds. The seed capsule of the ice plant is also a bilayer-like structure composed of an unresponsive valve and an active hygroscopic keel, which is able to unfold to achieve seed dispersal when sufficiently hydrated with water [14]. Inspired by the active bending phenomena of bilayers in nature, various engineered bilayers have been synthesized and utilized in developing soft robotics [6] and actuators [2]. A wide range of materials can be used as the actuation parts in bilayers, such

as thermo-responsive liquid crystal elastomers [15,16], thermo-responsive hydrogels [1,17,18], magneto-responsive bioinspired composites [5], and heat shrinkable polymer sheets [19]. Without losing their intrinsic physics, the various stimuli responsible for the actuation mechanism in bilayers are often modeled as prescribed active strains [9,20,21].

The bending behaviors of active bilayers have attracted great attentions, in particularly for the cases of two-dimensional (2D) bilayer beams under the condition of small deformations. In a pioneering work of this problem, Stoney revealed a linear relation between the curvature and the film stress in metal deposited film–substrate bilayers [22]. Later, Timoshenko studied the relation between bending curvature and stress distribution in 2D bi-metal thermostats upon heating [21]. His solution can be reduced to the Stoney's one when the top film of the bilayer is much thinner than its substrate. Earlier experimental and theoretical explorations on this topic can refer to the literature [23]. More recently, the two classical theories have been extended to analyze the relation between bending curvature, stress and active strain, including the cases with nonuniform substrate thicknesses and misfit strains [24], multi-layer thin films deposited on a substrate [7], nanosized bilayers with surface stresses [25], bilayers with thin substrates and large deformations [26], as well as pre-stretch bilayers [27].

* Corresponding author at: Laboratory for Soft Machines & Electronics, School of Packaging, Michigan State University, East Lansing, MI 48824, USA.

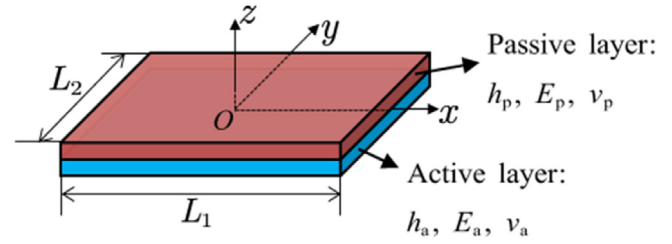
E-mail address: ccao@msu.edu (C. Cao).

In the bending of a three-dimensional (3D) active bilayer plate, bifurcation may occur, transitioning the bilayer from a spherical shape to a cylindrical one [28]. In Masters and Salamon's work, they systematically investigated the bending of free, rectangular, isotropic and thin bilayers by using both theoretical and finite element (FE) methods [8,29,30]. In addition, much efforts have been directed toward understanding the bifurcation phenomena based on different bilayer geometries, such as circular bilayers [10], thin rectangular bilayers with preferential bending [31], polygon bilayers [32] and thin sheets of arbitrary shapes under isotropic in-plane expansion [33]. By applying the energy method, the effects of layer geometry, plasticity and compositional gradient on the bifurcation points have been examined [34]. Recently, a non-Euclidean theory was presented to model the bending and twisting behaviors of bilayer structures, in which the strain components were defined as the fundamental forms of a deformed surface to describe arbitrary large rotation of the bilayer [35,36].

The bistability of bilayers under large active strain has technologically important applications in the design of bistable actuators with fast speed, large output force and binary-state switch [37, 38]. For instance, a square bilayer with isotropic active strains may evolve into a state with two stable cylindrical equilibrium shapes after shape bifurcation [8,28]. The bistability of square bilayers under active surface stresses could be controlled by two dimensionless parameters [39]. Alben et al. found that two stable equilibria did exist in a rectangular active bilayer and the spiral state was energetically preferred [31]. Although significant progress on the self-bending of bilayers has been made over the years, two fundamental problems remain unsolved: how is the bistability of a bilayer determined by the active strains? and how can we utilize active strains to achieve a highly efficient and optimal actuation? The answers to these questions can help design efficient bilayer-based bistable actuators and implement fast shape transition (i.e., snap-through) via active strain modulation. It is also useful to explain the bending/unbending phenomena encountered in bilayer structures in nature and to invent biomimetic materials and structures with improved functions. Additionally, the effect of anisotropic active strains has been addressed recently [40,41], however, the influence of anisotropic strains on the bistability transition remains unclear. The bending of 3D bilayers cannot be analyzed directly by the traditional Timoshenko's solution, which has been used for bilayer beams [42, 43].

In this paper, we study the bending behavior of a rectangular 3D bilayer plate by using the energy method and a Riks-based FE method. Similar to previous works reported [8,10,26,29,35,39,44], we employ a linear elastic constitutive model to characterize the material behaviors for the active strain less than 10%. The traditional Timoshenko's solution for a bilayer beam is extended to the case of large active strain by introducing the nonlinear effect of the axial stretch on the bending curvature in the formulation. The theoretical and numerical results are compared to examine the accuracy of the bilayer model. The snap-through instability and the critical transition from bistable state to monostable state have been analyzed using a two-loading-stage strategy in the FE procedure. A phase diagram for determining the bistability of a bilayer structure under different geometrical parameters and material properties has been presented. The methods for achieving snap-through and the optimal actuation for the bilayer are discussed.

This paper is organized as follows. In Section 2, we introduce the theoretical and numerical methods for analyzing active bilayers. In Section 3, the bending behaviors of bilayer beams and plates are studied. The phase transition of bistability and the corresponding snap-through behaviors for a representative bilayer are then discussed. In Section 4, the phase diagrams for determining the bistability and monostability states of the bilayer are presented and the optimal actuation strategies are summarized. Finally, concluding remarks are given in Section 5.



h —thickness, E —elastic modulus, ν —Poisson's ratio

Fig. 1. Schematic illustration of a bilayer structure.

2. Model

2.1. Formulation

To analyze the bending of a bilayer structure, we develop a theoretical model based on the minimization of free energy [10, 30]. The following assumptions are made: (1) the material is linear elastic because the considered 3D bending cases have active strains less than 10%; (2) the thickness of the bilayer is much smaller than its width and length such that the stress components in the thickness direction are ignored; (3) the interface of the two layers is perfectly bonded; (4) no wrinkle emerges on the bilayer surface; and (5) only the active strain components in the in-plane directions are considered. The strain energy function of the bilayer structure (Fig. 1) can be expressed as

$$U = \frac{1}{2} \int_{-\frac{L_2}{2}}^{\frac{L_2}{2}} \int_{-\frac{L_1}{2}}^{\frac{L_1}{2}} \left(\int_{-h_a}^0 \boldsymbol{\varepsilon}_a : \mathbf{C}_a : \boldsymbol{\varepsilon}_a dz + \int_0^{h_p} \boldsymbol{\varepsilon}_p : \mathbf{C}_p : \boldsymbol{\varepsilon}_p dz \right) dx dy \quad (1)$$

where \mathbf{C} is the elastic constitutive tensor with components $C_{ijkl} = 2\mu\delta_{ik}\delta_{jl} + \frac{2\mu\lambda}{2\mu+\lambda}\delta_{ij}\delta_{kl}$, μ and λ are Lamé's constants, $\boldsymbol{\varepsilon}$ is the elastic strain tensor, the subscripts 'a' and 'p' represent quantities of the active and passive layers, respectively, L_1 , L_2 and h are the dimensions of the bilayer structure (Fig. 1). For convenience of calculation, the plane $z = 0$ is set at the interface of the two layers. The strain tensors in the passive and active layers are, respectively, defined as

$$\boldsymbol{\varepsilon}_p = \frac{1}{2}(\mathbf{a} - \mathbf{I}) - z\mathbf{b}, \quad \boldsymbol{\varepsilon}_a = \frac{1}{2}(\mathbf{a} - \mathbf{I}) - z\mathbf{b} - \boldsymbol{\alpha} \quad (2)$$

where \mathbf{a} and \mathbf{b} are the first and second fundamental forms of the bilayer, respectively, and are defined as [45]

$$\mathbf{a} = \begin{bmatrix} \mathbf{r}_x \cdot \mathbf{r}_x & \mathbf{r}_x \cdot \mathbf{r}_y \\ \mathbf{r}_y \cdot \mathbf{r}_x & \mathbf{r}_y \cdot \mathbf{r}_y \end{bmatrix}, \quad \mathbf{b} = \begin{bmatrix} \mathbf{r}_{xx} \cdot \mathbf{n} & \mathbf{r}_{xy} \cdot \mathbf{n} \\ \mathbf{r}_{yx} \cdot \mathbf{n} & \mathbf{r}_{yy} \cdot \mathbf{n} \end{bmatrix}, \quad (3)$$

$$\mathbf{n} = \frac{\mathbf{r}_x \times \mathbf{r}_y}{\|\mathbf{r}_x \times \mathbf{r}_y\|}$$

where $\mathbf{r} = \mathbf{r}(x, y)$ is the parametric equation for characterizing the deformed shape of the bilayer, \mathbf{n} is the unit vector normal to the surface, \mathbf{r}_{ij} represents the derivatives of \mathbf{r} with respect to the coordinates, e.g., $\mathbf{r}_x = \frac{\partial \mathbf{r}}{\partial x}$, $\mathbf{r}_{xx} = \frac{\partial^2 \mathbf{r}}{\partial x^2}$. $\boldsymbol{\alpha} = \text{diag}(\alpha_x, \alpha_y)$ is the active strain whose components α_x and α_y are assumed to be uniformly distributed, \mathbf{I} is the identity tensor. The shear components of $\boldsymbol{\alpha}$ are not considered in this work, which may induce helical shapes for the bilayers with large length-to-width ratios [44].

As for the deformed shape of a bilayer, some researchers have employed polynomial [10,23,30] or parametric equations [39] to approximate its deformed shape. Here, we construct a four-parameter equation $\mathbf{r} = \mathbf{r}(x, y)$ through a composition of two

circular parametric equations in the x and y directions

$$\mathbf{r} = \mathbf{r}(x, y) = \left\{ r_1 \sin\left(\frac{\lambda_1 x}{r_1}\right), r_2 \sin\left(\frac{\lambda_2 y}{r_2}\right), r_1 + r_2 - r_1 \cos\left(\frac{\lambda_1 x}{r_1}\right) - r_2 \cos\left(\frac{\lambda_2 y}{r_2}\right) \right\}^T \quad (4)$$

where λ_1 and λ_2 are the stretches in the x and y directions, r_1 and r_2 are the corresponding radii of the circles. In Eq. (4), the effects of the axial stretches λ_1 and λ_2 on the deformation are considered, which will facilitate the accurate characterization of the large bending behaviors of the bilayer. The reduced form of Eq. (4) in the 2D case is the parametric equation of a circle, which accurately describes the deformed shape of a 2D bilayer beam. Substituting Eq. (4) into (3), \mathbf{a} and \mathbf{b} can be obtained as

$$\mathbf{a} = \begin{bmatrix} \lambda_1^2 & \lambda_1 \lambda_2 \sin\left(\frac{\lambda_1 x}{r_1}\right) \sin\left(\frac{\lambda_2 y}{r_2}\right) \\ \lambda_1 \lambda_2 \sin\left(\frac{\lambda_1 x}{r_1}\right) \sin\left(\frac{\lambda_2 y}{r_2}\right) & \lambda_2^2 \end{bmatrix}, \quad \mathbf{b} = \begin{bmatrix} \frac{\lambda_1^2}{r_1 f_b} \cos\left(\frac{\lambda_2 y}{r_2}\right) & 0 \\ 0 & \frac{\lambda_2^2}{r_2 f_b} \cos\left(\frac{\lambda_1 x}{r_1}\right) \end{bmatrix} \quad (5)$$

where

$f_b = \sqrt{-\cos^2\left(\frac{\lambda_1 x}{r_1}\right) \cos^2\left(\frac{\lambda_2 y}{r_2}\right) + \cos^2\left(\frac{\lambda_1 x}{r_1}\right) + \cos^2\left(\frac{\lambda_2 y}{r_2}\right)}$. It can be proved that \mathbf{a} and \mathbf{b} satisfy the Gauss–Codazzi equations [45] and thus are geometrically compatible.

Since the energy functional in Eq. (1) is integrable, we express $\boldsymbol{\varepsilon}$ (excluding $\boldsymbol{\alpha}$) through the first-order approximation:

$$\boldsymbol{\varepsilon} = \begin{bmatrix} \varepsilon_1 & 0 \\ 0 & \varepsilon_2 \end{bmatrix} - z \begin{bmatrix} (2\varepsilon_1 + 1)\kappa_1 & 0 \\ 0 & (2\varepsilon_2 + 1)\kappa_2 \end{bmatrix} \quad (6)$$

and the third-order expansion at the origin (0, 0)

$$\boldsymbol{\varepsilon} = \begin{bmatrix} \varepsilon_1 & xy\kappa_1\kappa_2(2\varepsilon_1 + 1)(2\varepsilon_2 + 1) \\ xy\kappa_1\kappa_2(2\varepsilon_1 + 1)(2\varepsilon_2 + 1) & \varepsilon_2 \end{bmatrix} - z \begin{bmatrix} \kappa_{xx} & 0 \\ 0 & \kappa_{yy} \end{bmatrix} \quad (7)$$

where the axial strain components satisfy $\varepsilon_1 = \frac{1}{2}(\lambda_1^2 - 1)$, $\varepsilon_2 = \frac{1}{2}(\lambda_2^2 - 1)$, and the curvature components $\kappa_1 = \frac{1}{r_1}$, $\kappa_2 = \frac{1}{r_2}$, $\kappa_{xx} = -\frac{1}{2}\kappa_1\kappa_2^2y^2(2\varepsilon_1 + 1)(2\varepsilon_2 + 1) + (2\varepsilon_1 + 1)\kappa_1$, and $\kappa_{yy} = -\frac{1}{2}\kappa_2\kappa_1^2x^2(2\varepsilon_1 + 1)(2\varepsilon_2 + 1) + (2\varepsilon_2 + 1)\kappa_2$. From Eq. (5), it can be verified that the principal curvatures at the origin (0, 0, 0) are κ_1 and κ_2 . Note that ε_1 , ε_2 , κ_1 , and κ_2 are measured at the interface between the two layers, i.e., $z = 0$.

As another feasible route to obtain an integrable functional, we can substitute Eq. (5) into Eqs. (1) and (2), and then perform a Taylor series expansion on the entire integrand. After substituting Eq. (7) into (1), an energy functional defined with regard to ε_1 , ε_2 , κ_1 , and κ_2 can be obtained. A derivative with respect to the four parameters leads to the equilibrium equations

$$\frac{\partial U}{\partial \varepsilon_1} = 0, \quad \frac{\partial U}{\partial \varepsilon_2} = 0, \quad \frac{\partial U}{\partial \kappa_1} = 0, \quad \frac{\partial U}{\partial \kappa_2} = 0 \quad (8)$$

The stability of the solution can be determined by the determinant of the Hessian matrix of U [46].

2.2. Numerical method

We implement the elastic constitutive equation in the previously developed Riks method-based finite element (FE) procedure [47] to simulate the bending of the bilayer

$$\mathbf{S} = \mathbf{C} : (\mathbf{E} - \boldsymbol{\alpha}) \quad (9)$$

where \mathbf{S} is the second Piola–Kirchhoff stress, \mathbf{E} is the Green strain, and \mathbf{C} and $\boldsymbol{\alpha}$ are linearly elastic constitutive tensor and the active strain, respectively. The FE analysis permits the characterization of large bending deformation with nonuniform distribution of strain and curvature, and the Riks method provides advantages to precisely capture the phase boundary (PB) and critical shapes before and after shape transition (i.e., snap-through). If bending contribution $z\mathbf{b}$ in the strain tensor in Eq. (2) is ignored, it reduced to the strain at $z = 0$ and has the same form as the Green strain \mathbf{E} . Therefore, the constitutive models used in the analytical and numerical analysis are compatible with each other. In simulation, $\boldsymbol{\alpha}$ increases incrementally following $\boldsymbol{\alpha} = \delta\bar{\boldsymbol{\alpha}}$, where δ is a scalar characterizing the magnitude of $\boldsymbol{\alpha}$ and $\bar{\boldsymbol{\alpha}} = \text{diag}(\bar{\alpha}_1, \bar{\alpha}_2)$ is a fixed pattern tensor characterizing its distribution. If uniform active strain is considered, $\bar{\alpha}_1$ and $\bar{\alpha}_2$ are constants in the active layer.

The linearized balanced equation in the FE procedure can be generally expressed as [47]

$$\mathbf{K}\Delta\mathbf{w} = \Delta\delta\mathbf{f}^s - \mathbf{f}^{\text{int}} \quad (10)$$

where $\Delta\mathbf{w}$ and $\Delta\delta$ are increments of the displacement vector and the scalar factor to be solved, \mathbf{K} is the stiffness matrix, \mathbf{f}^{int} is the internal force, and \mathbf{f}^s is an equivalent body force induced by the pattern tensor $\bar{\boldsymbol{\alpha}}$. The balance equation is solved by combining a supplementary arc-length equation

$$\Delta\mathbf{w} \cdot \Delta\mathbf{w} + \Delta\delta^2 = \rho^2 \quad (11)$$

where ρ is the arc length. Compared to the traditional Newton–Raphson scheme, the step size is controlled by ρ rather than by a prescribed change in the history of the scalar factor δ . It can be conferred that the total equivalent body force $\Delta\delta\mathbf{f}^s$ in the linearized equation plays a role in driving the deformation of the bilayer. Thus, within the solution scheme, the scalar factor δ and the displacement vector are updated automatically, which enables tracking of the nonmonotonic equilibrium path during the snap-through process [47,48]. From the simulated relation between the active strain and deformed shape, we can identify the location of the limit point, where the change rate of the active strain is vanished and can thus precisely determine the critical active strain for the transition from bistability to monostability. In the calculations, eight-nodes quadrilateral and twenty-nodes hexagonal elements are developed in our in-house codes to model 2D and 3D problems, respectively.

3. Representative solutions for bilayer structures

3.1. 2D bilayer beams

For bilayer beams, the parametric Eq. (4) can be simplified as $\mathbf{r} = \mathbf{r}(x) = \left\{ r_1 \sin\left(\frac{\lambda_1 x}{r_1}\right), 0, r_1 - r_1 \cos\left(\frac{\lambda_1 x}{r_1}\right) \right\}^T$, representing a perfect circular arc. The nonvanishing strain component in Eq. (6) becomes $\varepsilon_{xx} = \varepsilon_1 - z\kappa_1(2\varepsilon_1 + 1) = \varepsilon_1 - z\kappa_1\lambda_1^2$. It is noted that a direct calculation based on Eq. (3) can also obtain the same ε_{xx} in this case. Since ε_{xx} depends on the z -coordinate, we calculate the integration in Eq. (1) in the z direction, and let its derivatives with respect to ε_1 and κ_1 vanish. Then, we obtain the

nondimensionalized curvature

$$\begin{aligned}\bar{\kappa}_M &= \kappa_1 h \\ &= \frac{6\alpha mn(1+n)^2}{m^2 n^4 + 4mn^3 + 6mn^2 + 4mn + 1 + 8\alpha mn^3 + 6\alpha mn^2 + 2\alpha}\end{aligned}\quad (12)$$

and the corresponding axial strain

$$\varepsilon_M = \frac{\alpha(4mn^3 + 3mn^2 + 1)}{m^2 n^4 + 4mn^3 + 6mn^2 + 4mn + 1}\quad (13)$$

where the nondimensional parameters satisfy $m = \frac{E_p}{E_a}$, $n = \frac{h_p}{h_a}$, and $h = h_1 + h_2$ is the total thickness of the bilayer. In the case of small ε_1 , ε_{xx} is simplified as $\varepsilon_{xx} = \varepsilon_1 - z\kappa_1$. Then, based on the same procedure, we obtain the Timoshenko's solution [21]

$$\bar{\kappa}_T = \frac{\kappa_T h}{\alpha} = \frac{6mn(1+n)^2}{m^2 n^4 + 4mn^3 + 6mn^2 + 4mn + 1}, \quad \varepsilon_T = \varepsilon_M\quad (14)$$

It can be seen that Eq. (12) will reduce to the Timoshenko's solution in Eq. (14) when α in the denominator of Eq. (12) is set to be zero. Therefore, these additional terms are induced by the effect of axial stretch λ_1 on the curvature κ_1 . As shown in Figs. 2a and b, the modified curvature in Eq. (12) shows significant discrepancies with the Timoshenko's solution, especially for large values of α . When $|\alpha| < 5\%$, the two groups of solutions are almost identical. The FE solutions show a better agreement with the new modified solutions than the Timoshenko's solutions for the entire range of α , indicating the validity of Eq. (12). For the Timoshenko's solution, the curvature changes linearly with α , while the modified one varies nonlinearly. Also, if the same degrees of expansion or shrinkage are applied in the active layer, the Timoshenko's solution will predict an equal bending degree for the bilayer, while the modified solution will give a larger bending degree in expansion than that in shrinkage. In the case $\alpha > 0$, it can be seen from Eqs. (12)~(14) or Fig. 2a and b that the modified solution has a smaller curvature than the Timoshenko's solution, which means that the former one predicts a larger bending degree than the latter one due to the effects of the axial strain, and vice versa.

With the analytical solution Eq. (12), we can determine the parameters m and n for the largest bending degree. Taking the derivative with respect to m in Eq. (12), it is demonstrated that $\bar{\kappa}_M$ reaches the maximum value when $mn^2 = \sqrt{2\alpha + 1}$. In real applications, it is difficult to adjust the material constants m and n to meet the condition of $mn^2 = \sqrt{2\alpha + 1}$, because α varies during the deformation process. To obtain a usable optimal solution for realistic applications, we assume α is small and taken a derivative with respect to m in Eq. (14), then it can be proved that $\bar{\kappa}_T$ gets its maximum value, $\bar{\kappa}_{T, \max} = 1.5$, when $mn^2 = 1$ (or $\log(mn^2) = 0$ or $E_1 h_1^2 = E_2 h_2^2$). Thus, to achieve the most efficient actuation (the largest bending degree), the material parameter Eh^2 should be equal in the active and passive layers. The distribution of $\bar{\kappa}_T$ in Fig. 2c also verifies the same results. Recently, Kim et al. investigated the bending of hydrogel bilayers with different thickness ratios [43], and they found that the sample with equal thickness provides the largest bending curvature, i.e., $h_1 \approx h_2$. They used the same kind of hydrogels in the passive and active layers, so the bilayer has almost equal modulus in each layer, i.e., $E_1 \approx E_2$. In their experiments, the case of $E_1 h_1^2 = E_2 h_2^2$ described in our analysis was further demonstrated to give an optimal bending performance. However, experimental demonstrations for other cases with both different E and h are still lacking.

3.2. 3D bilayer plates

In this case, a square-shaped bilayer plate with $L_1 = L_2 = L$ is considered. By introducing the variables $m = \frac{E_p}{E_a}$, $n = \frac{h_p}{h_a}$, $p = \frac{L}{h} = \frac{L}{h_1 + h_2}$ and a parameter assemble $\zeta = (m, n, p, \nu_a, \nu_p)$, the energy functional in Eq. (1) is expressed in a nondimensionalized form as

$$\bar{U} = \frac{U}{EL^2 h} = \bar{U}(\varepsilon_1, \varepsilon_2, \bar{\kappa}_1, \bar{\kappa}_2, \zeta, \alpha)\quad (15)$$

where $E = (E_a + E_p)/2$ and $\bar{\kappa} = \kappa h$. Based on the first order approximation of the strain in Eq. (6), we can obtain analytical solutions for certain specific cases. We first consider the spherical case before the shape bifurcation, where isotropic active strains are present in the structure and the curvature has uniform distribution, i.e., $\alpha_1 = \alpha_2 = \alpha$ and $\kappa_1 = \kappa_2 = \kappa_0$, $\varepsilon_1 = \varepsilon_2 = \varepsilon_0$. Note that in this case m is defined by $m = \frac{\bar{E}_p}{\bar{E}_a}$ with $\bar{E}_p = \frac{E_p}{1-\nu_p}$, $\bar{E}_a = \frac{E_a}{1-\nu_a}$, so that we can eliminate the Poisson's ratio ν in Eq. (15). Based on the standard minimization procedure of elastic strain energy, we obtain

$$\begin{aligned}\bar{\kappa}_0 &= \kappa_0 h \\ &= \frac{6\alpha mn(1+n)^2}{m^2 n^4 + 4mn^3 + 6mn^2 + 4mn + 1 + 8\alpha mn^3 + 6\alpha mn^2 + 2\alpha}\end{aligned}\quad (16)$$

$$\varepsilon_0 = \frac{\alpha(4mn^3 + 3mn^2 + 1)}{m^2 n^4 + 4mn^3 + 6mn^2 + 4mn + 1}\quad (17)$$

It is found that $\bar{\kappa}_0$ and ε_0 have the same form as those in Eqs. (12) and (13) for the 2D bilayer beam except the difference of m value. If we set $\alpha = 0$, Eq. (16) will reduce to that obtained by Finot and Suresh [34] or Freund and Suresh [23], where a linear relation between $\bar{\kappa}_0$ and α was found like in the Timoshenko's solution. They made a detailed discussion of the effects of m and n on the curvature $\bar{\kappa}_0$ [34]. However, the spherical shape only exists for relatively small α before bifurcation occurs at the curvature $\bar{\kappa}_0 \sim \frac{h^2}{L^2}$ [8]. Thus, the linear $\bar{\kappa}_0$ should be accurate enough to characterize the bending at this stage [34].

For anisotropic active strains with $\alpha_1 = \alpha$, $\alpha_2 = 0$ and $\nu_p = \nu_a$, the curvatures can be obtained as

$$\begin{aligned}\bar{\kappa}_1 &= \kappa_1 h \\ &= \frac{6\alpha mn(1+n)^2}{m^2 n^4 + 4mn^3 + 6mn^2 + 4mn + 1 + 8\alpha mn^3 + 6\alpha mn^2 + 2\alpha}, \\ \bar{\kappa}_2 &= 0\end{aligned}\quad (18)$$

It is noted that Eq. (18) is the same as Eq. (12) for the bilayer beam. When $\nu_p \neq \nu_a$, we can prove that $\bar{\kappa}_2 = 0$, but the lengthy expression of $\bar{\kappa}_1$ is omitted here. Fig. 3a shows the curvatures obtained by the different methods for the case of anisotropic active strains. In the FE solution, the curvature is calculated by using the least square method based on the coordinates of eight neighbor nodes of the origin $(x, y, z) = (0, 0, 0)$ (Fig. 1). Three groups of FE results with different combinations of the Poisson's ratios are presented in the figure, which are almost identical, indicating that the Poisson's ratio has little effect on the bending curvature for the case of anisotropic active strain. Therefore, in the following calculations, we take the Poisson's ratio as $\nu_p = \nu_a = 0.49$ in all situations. The theoretical results in Eq. (18) show a good agreement with FE results, while a large deviation from the linear solution can be observed for large active strains.

For more general cases, we employ the third-order approximation in Eq. (7) and can obtain four nonlinear equations from Eq. (8) to solve κ_1 , κ_2 , ε_1 and ε_2 numerically. Fig. 3b shows the

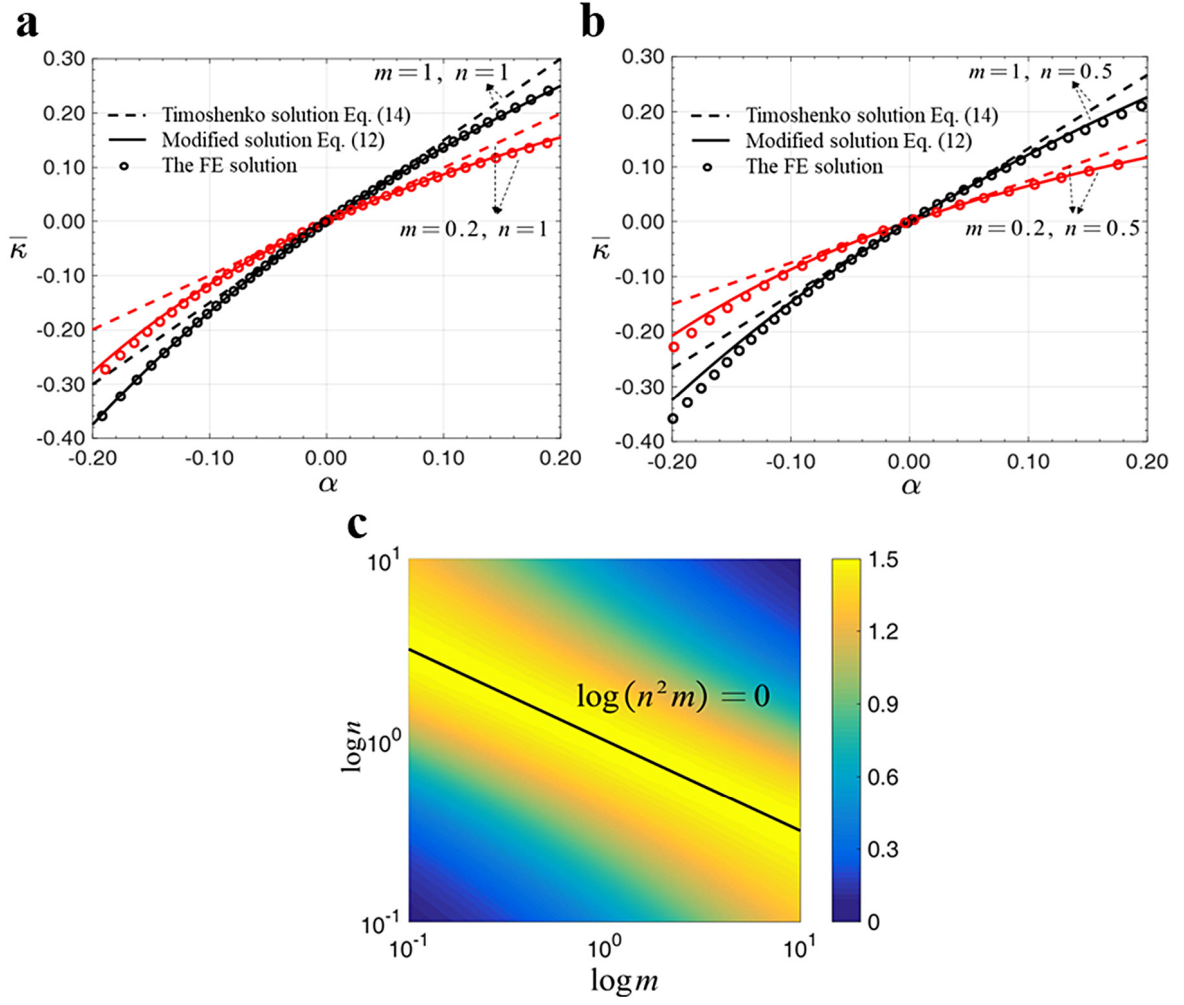


Fig. 2. Comparison of the modified solution with FE solution and traditional Timoshenko solution. (a–b) Comparisons of the curvature $\bar{\kappa}$ versus the active strain α for different $m = E_p/E_a$ and $n = h_p/h_a$ in 2D bilayer beam. (c) The distribution of Timoshenko's solution $\bar{\kappa}_T$ with respect to m and n . When $\log(mn^2) = 0$ (i.e., $mn^2 = 1$ or $E_1 h_1^2 = E_2 h_2^2$), $\bar{\kappa}_T$ takes the maximum value $\bar{\kappa}_{T,\max} = 1.5$.

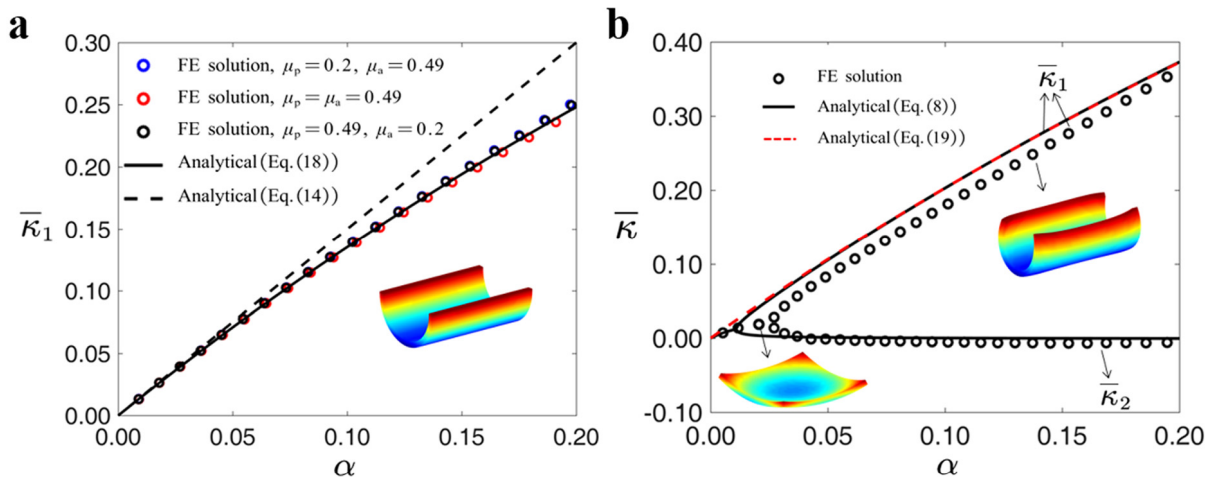


Fig. 3. Comparison of the theoretical and FE solutions for bending curvature of a 3D bilayer plate, including (a) the anisotropic ($\alpha_1 = \alpha, \alpha_2 = 0$) and (b) the isotropic active strains ($\alpha_1 = \alpha_2 = \alpha$). The other parameters for the calculations are $m = n = 1, p = 20$.

theoretical and FE results for the special case with isotropic active strains of $\alpha_1 = \alpha_2 = \alpha$. The shape bifurcation from a spherical shape ($\bar{\kappa}_1 = \bar{\kappa}_2$) to a cylindrical shape ($\bar{\kappa}_1 > \bar{\kappa}_2 \approx 0$) can be

observed from both the results of theoretical analysis and FE simulations. It can be easily inferred that another stable state $\bar{\kappa}_1 > \bar{\kappa}_2 \approx 0$ exists due to the symmetry of the bilayer. The bending

curvatures after bifurcation show a reasonable agreement between the two methods. This indicates that the theoretical model captures the basic features of the bending process of the bilayer despite the difference in the location of the bifurcation point. The error in the theoretical analysis may arise from the assumption of the strain distribution (Eq. (2)) and the deformed shape (Eq. (5)), which cannot precisely characterize the out-of-plane shear strain at large bending curvature and the non-uniform distribution of the curvature [10,23,31,49] along the edges of the bilayer.

If we assume $\bar{\kappa}_2 = 0$ and $v_a = v_p = v$, the curvature in the x direction can be obtained as

$$\bar{\kappa}_1 = \kappa_1 h = \frac{6\alpha mn(1+v)(1+mn)(1+n)^2}{C(m, n, v, \alpha)} \quad (19)$$

where

$$C = m^3 n^5 + 5m^2 n^4 + 4m^3 n^3 + 4m^2 n^2 + 4mn^3 + 6mn^2 + 5mn + 1 + \alpha(6m^2 n^3 + 8m^2 n^4 + 2mn + 6mn^2 + 8mn^3 + 2) + 6\alpha v(-mn - mn^2 + m^2 n^3 + m^2 n^4)$$

As shown in Fig. 3b, Eq. (19) is able to characterize the evolution of $\bar{\kappa}_1$ well at large active strains and thus can serve as a good estimation for the bending curvature after the bifurcation under isotropic active strains.

3.3. Phase transition in the bending process

The bending behaviors of a bilayer structure for two special active strains are discussed in the previous sections, i.e., the isotropic one with $\alpha_1 = \alpha_2$ and the anisotropic one with $\alpha_1 \neq \alpha_2 = 0$. From the analysis, we have found that a square bilayer with isotropic active strains has two stable states after buckling. Thus, it is interesting to check the conditions for the bistability of a bilayer subjected to arbitrary active strains. Since the analytical solution may induce significant errors in the analysis for these problems due to the approximation of parametric shapes (Fig. 3b), especially for more complicated cases, we will employ the Riks method-based FE procedure to predict the bending behaviors of the bilayer. In the FE procedure described in Section 2, the displacement and the scalar factor δ are updated automatically after the pattern tensor $\bar{\alpha}$ is given. To capture the phase transition from bistability to monostability, we assign different $\bar{\alpha}$ in two loading steps, that is, stage 1: isotropic expansion with $\bar{\alpha}_1 = \bar{\alpha}_2 = 1$, and stage 2: anisotropic expansion or shrinkage in the y direction with $\bar{\alpha}_1 = 1$ or -1 and $\bar{\alpha}_2 = 0$.

A square bilayer is first considered with the parameters $m = n = 1$ and $p = 20$. The evolutions of $\bar{\kappa}_1$ and $\bar{\kappa}_2$ in the two loading stages are plotted in Fig. 4a and b, respectively, where the method of computing $\bar{\kappa}$ is the same as that used in Fig. 3. At the initial step with $\alpha_1 = \alpha_2 < 0.026$, the bilayer shows a spherical shape with $\bar{\kappa}_1 = \bar{\kappa}_2$. Then at point A, it bifurcates into a cylindrical shape with $\bar{\kappa}_1 > \bar{\kappa}_2 \approx 0$ until the end of the first loading stage at point B (total of 60 increment steps in the first loading stage). In the second loading stage, α_1 increases or decreases based on the value of $\bar{\alpha}_1$ assigned in the simulation, while α_2 is kept as a constant of 0.073. If $\bar{\alpha}_1 = 1$, the bilayer continues to bend to a large degree as shown in blue lines and configuration F in Fig. 4. If $\bar{\alpha}_1 = -1$, α_1 shows a nonmonotonic change (the red lines). It first decreases until point C ($\alpha_1 = 0.043$), then it increases to the point D ($\alpha_1 = 0.173$), and finally it decreases again. If α_1 keeps decreasing at point C, the bilayer jumps from configuration C to E, with a reverse in the bending direction. Similarly, the bilayer snaps from configuration D to F if α_1 continues to increase at point D. The point C or D on the equilibrium path is known as the limit point, where the change rate of the active strain is vanishing [47,48]. The active strains at

points C and D, i.e., $(\alpha_1, \alpha_2) = (0.043, 0.073)$ and $(0.173, 0.073)$, are the critical values where the phase transition from bistability to monostability of the bilayer occurs. It can be found that the structure has two stable paths (excluding the unstable path from C to D) when $\alpha_1 \in [0.043, 0.173]$, while it has only one stable path for other values of α_1 . In Fig. 4b, the energy sketches are plotted at several representative points. In the bistable region, the energy curve presents two local minima (e.g., S1 and S2 at point B), while at PB one of the local minima evolves into a metastable point (e.g., state S2 at point C or state S1 at point D). Given a small perturbation to the bilayer at state S2 of point C, it exhibits a sharp shape jump from state S2 to S1. The evolution of the nominal strain energy (Eq. (15)) in Fig. 4d indicates that the snap-through process involves a strain-energy release from high-energy states (C and D) to low energy states (E and F). It is noticed that the shape transition at the PB II releases more energy than that at PB I, since it needs a larger active strain to trigger the snap-through instability.

From the representative results, we can conclude that the snap-through instability of a bilayer only occurs at the PBs. This is a requisite to realize achievable bilayer-based actuators with shape jump. The specific active-strain route for triggering this process is dependent on the initial state of the bilayer. As shown in Fig. 4c with the two stable equilibrium paths plotted simultaneously, if the bilayer is initially in the state with $\bar{\kappa}_1 > \bar{\kappa}_2 \approx 0$ (the black lines), we need to decrease α_1 (shrinkage) to push the structure out of the bistable region and achieve shape jump at the PB I. On the contrary, if the bilayer has an initial state $\bar{\kappa}_2 > \bar{\kappa}_1 \approx 0$, increasing α_1 to the PB II leads to the snap-through to the state $\bar{\kappa}_1 > \bar{\kappa}_2 \approx 0$, but increasing α_2 or decreasing α_1 cannot realize this process. In the monostable region, the maximum curvature $\bar{\kappa}_{\max} = \max(\bar{\kappa}_1, \bar{\kappa}_2)$ for different α_1 and α_2 is easily identified, i.e., $\bar{\kappa}_{\max} = \bar{\kappa}_2$ when $\alpha_1 < 0.043$, and $\bar{\kappa}_{\max} = \bar{\kappa}_1$, when $\alpha_1 < 0.173$. In the bistable region, the larger curvature between the two can be identified directly from Fig. 4c. For the isotropic expansion with $\alpha_1 = \alpha_2 = 0.073$ (point P in Fig. 4c), the two stable states represent the same deformed shape. Also, it is noticed that $\bar{\kappa}_1 > \bar{\kappa}_2$ when $\alpha_1 > \alpha_2$, and vice versa (Fig. 4c).

Fig. 5a gives two other groups of $\bar{\kappa}_{\max}$ with $\alpha_2 = 0.049$ and 0.101. It can be seen that $\bar{\kappa}_{\max}$ increases with both α_1 and α_2 . To characterize the bending efficiency, we define the average curvature as

$$\tilde{\kappa} = \bar{\kappa}_{\max} / (\alpha_1 + \alpha_2) \quad (20)$$

which represents the bending degree per unit active strain approximately. For the 2D beam case, $\tilde{\kappa}$ is reduced to $\bar{\kappa}_M / \alpha$ (Eq. (12)). From Fig. 5b, $\tilde{\kappa}$ reaches its maximum value when $\alpha_1 = 0$ for all different choices of α_2 , while it goes to a minimum value when $\alpha_1 = \alpha_2$. The increase rate of $\tilde{\kappa}$ for $\alpha_1 < \alpha_2$ is much larger than that for $\alpha_1 > \alpha_2$. This means that the bilayer has the maximum bending efficiency for the anisotropic active strain with $\alpha_1 = 0$ and $\alpha_2 \neq 0$ and the minimum for the isotropic one with $\alpha_1 = \alpha_2$. The maximum $\tilde{\kappa}$ at $\alpha_1 = 0$ shows a deviation from 1.5, which should be induced by the nonlinear terms in the curvature expression in Eq. (18).

4. Phase diagram and optimal actuation for bilayer structures

The phase diagram of the bending behaviors of a bilayer and its optimal actuation for desired shapes are of great interest for exploring its applications. With the selected geometry and material properties, we have performed extensive numerical simulations for the active-strain actuated snap-through buckling in bilayer structures, and identified the corresponding phase transition boundaries and maximum bending curvature with respect

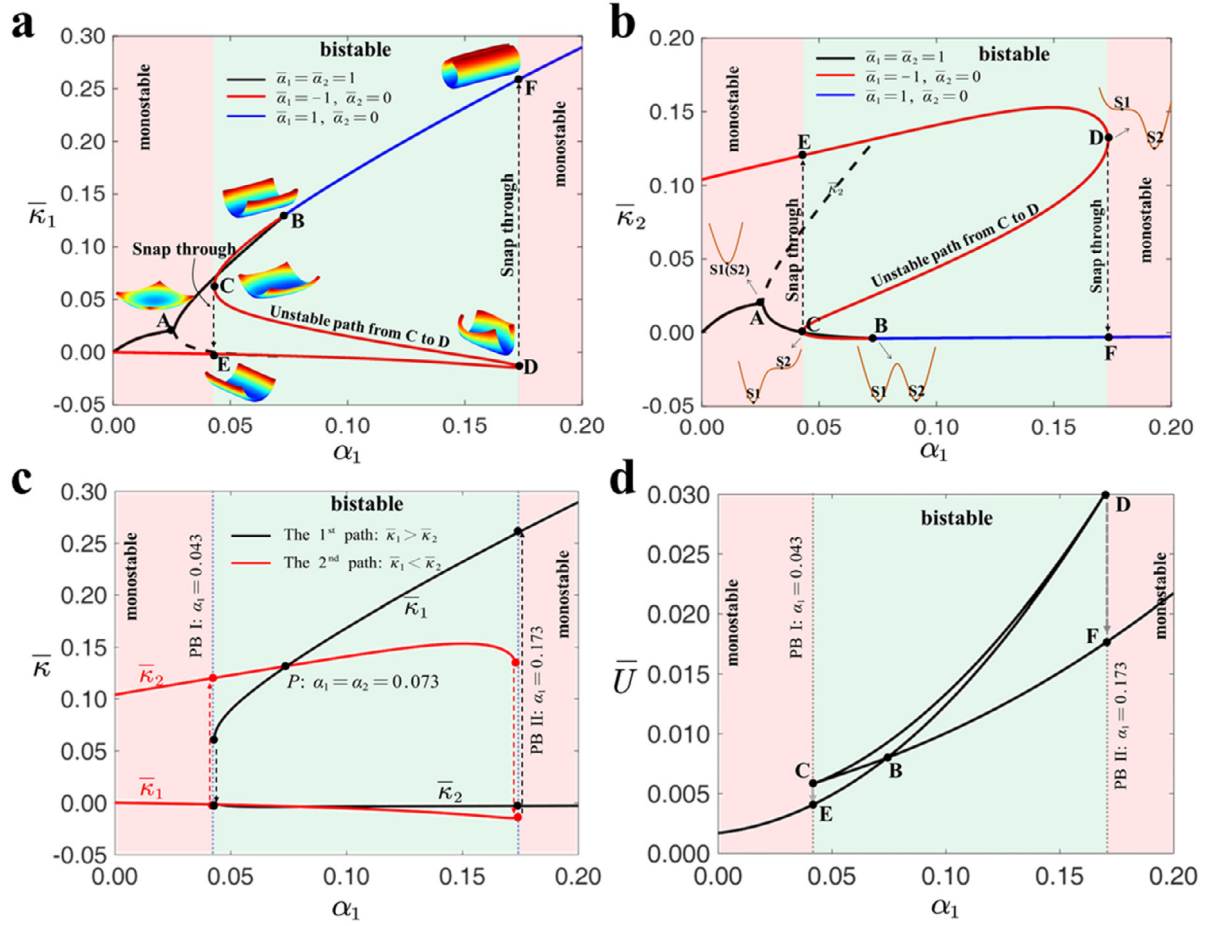


Fig. 4. Curvature evaluation and solution bifurcation for a square of bilayer under various active strains. (a–b) Evolution of $\bar{\kappa}_1$ and $\bar{\kappa}_2$ with respect to the active strain α_1 . The black lines are the results in the first loading stage with $\bar{\alpha}_1 = \bar{\alpha}_2 = 1$, and the blue and red lines are the results in second loading stage with $\bar{\alpha}_1 = 0$, and $\bar{\alpha}_2 = 1$ or -1 . The PBs are identified based on the curvature evolution in the second loading stage. (c–d) Evolution of the two equilibrium paths, i.e., $\bar{\kappa}_1 > \bar{\kappa}_2$ and $\bar{\kappa}_1 < \bar{\kappa}_2$, and the nominal strain energy, \bar{U} , with respect to α_1 in the second loading stage, where α_2 is fixed as 0.073. Other parameters are $m = n = 1$, $p = 20$. PB stands for the phase boundary. (For interpretation of the references to color in this figure legend, the reader is referred to the web version of this article.)

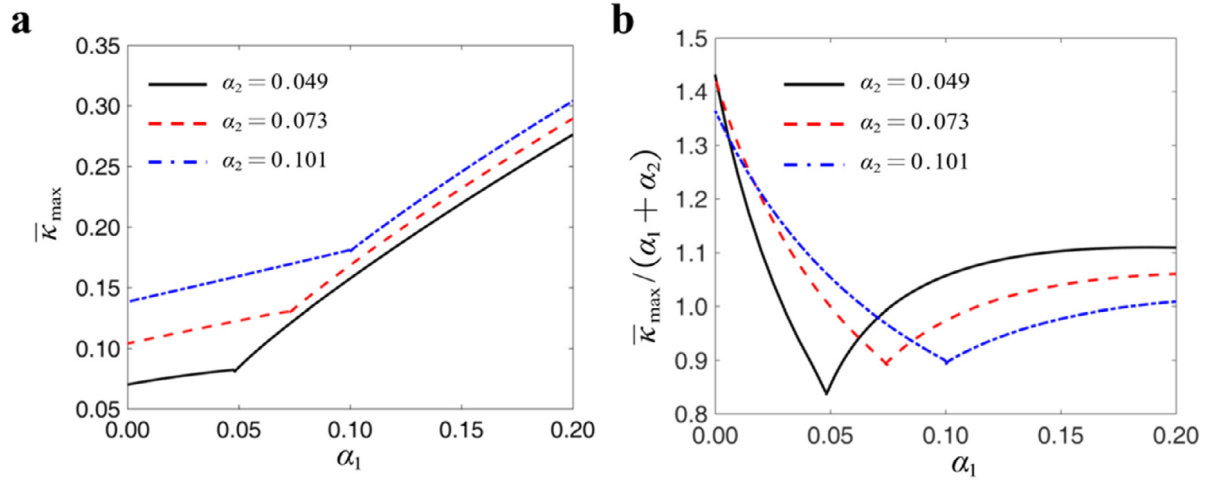


Fig. 5. Evolution of (a) the maximum curvature $\bar{\kappa}_{max}$ and (b) the average curvature $\bar{\kappa}_{max}/(\alpha_1 + \alpha_2)$ versus α_1 for different fixed α_2 . Other parameters are $m = n = 1$, $p = 20$. The inflection point on each curve represents the case with isotropic active strain, i.e., $\alpha_1 = \alpha_2$.

to various combinations of α_1 and α_2 . Fig. 6 presents the PBs for the bistability and the contour plot of $\bar{\kappa}_{max}$ and $\bar{\kappa}$. It can be seen that the phase point (α_1, α_2) in the bistable region (e.g. point A) corresponds to two stable configurations (Fig. 6a) and two energy

wells on the energy landscape (Fig. 6b). As the point shifts to the PB (e.g., point B), one stable configuration evolves into a meta-stable, and a small external perturbation leads to a shape jump from state S1 to the other state S2. In the monostable region, the

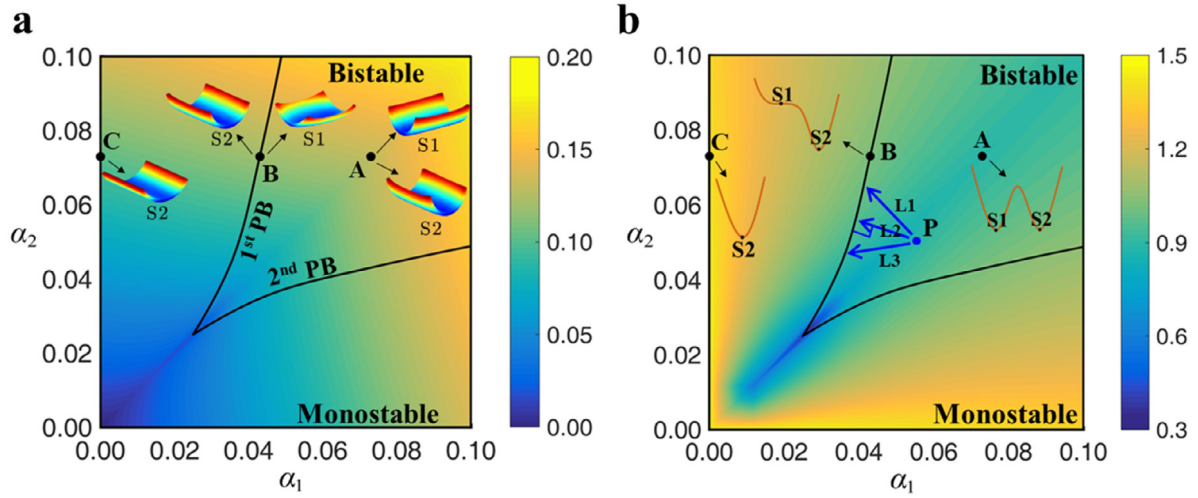


Fig. 6. Phase diagram for bistability of the bilayer structure with $m = n = 1$, $p = 20$. The distribution of (a) the maximum curvature $\bar{\kappa}_{\max}$ and (b) the average curvature $\bar{\kappa}$. The stable configurations and energy landscapes at points A (0.073, 0.073), B (0.043, 0.073), and C (0, 0.073) are presented in the plots. PB stands for the phase boundary.

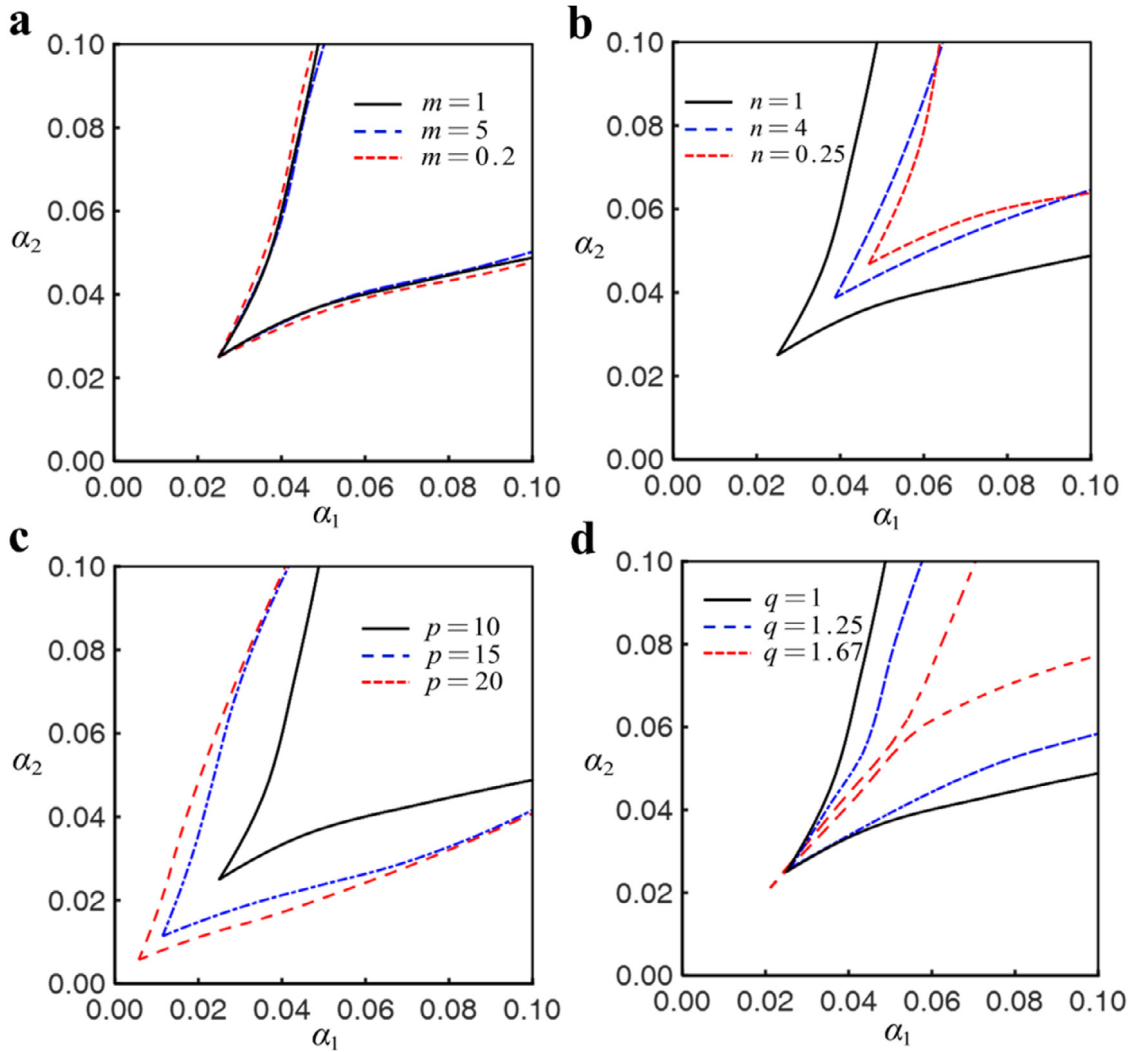


Fig. 7. The phase boundaries for the bistability of a bilayer for different (a) ratios of elastic moduli m , (b) ratios of thicknesses n , (c) overall sizes-to-thickness ratio p , and (d) length-to-width ratios q .

structure has only one stable state and a global minimum on the energy landscape (e.g., point C).

Without loss of generality, we take a state S1 with $\bar{\kappa}_1 > \bar{\kappa}_2$ as an example to demonstrate the guidelines for generating snap-through instability by choosing an optimal active-strain route. In

such a case, the only possible configuration after snap-through can be generally represented by state S2 with $\bar{\kappa}_1 < \bar{\kappa}_2$. Therefore, we vary α_1 and α_2 to make the phase point move across the first PB (Fig. 6a), at which the energy well of S1 disappears and the bilayer snaps to state S2 with $\bar{\kappa}_1 < \bar{\kappa}_2$. On the contrary, if the structure is in an initial state S2 with $\bar{\kappa}_1 < \bar{\kappa}_2$, we vary the values of α_1 and α_2 so as to move the phase point to the second PB to achieve snap-through. Nevertheless, no snap-through is involved at the PB if the phase point (α_1, α_2) is initially located in the monostable region. Therefore, shape evolution from the monostable region to the bistable region must be continuous. It can be easily concluded that, for an arbitrary phase point P with $\bar{\kappa}_1 > \bar{\kappa}_2$ in the bistable region, various active-strain routes exist to achieve snap-through on the 1st PB, such as L1, L2 and L3 shown in Fig. 6b. Among these routes, there exists a unique shortest route L2 perpendicular to the PB, which can be considered as the easiest way to generate snap-through from initial state P. Therefore, the phase diagram provides a guidance to achieve efficient shape jump for the bilayer-based, bistable actuators.

As depicted in the contour plot of Fig. 6, the maximum curvature $\bar{\kappa}_{\max}$ increases with both α_1 and α_2 while the average curvature $\bar{\kappa}$ assumes the maximum value when one component of the active strains is vanishing. These results are consistent with the analysis in Fig. 5. For instance, given an active-strain combination satisfying $\alpha_1 + \alpha_2 = \text{const}$, when $\alpha_1 = 0$ or $\alpha_2 = 0$, $\bar{\kappa}$ gets its maximum value, indicating that the anisotropic active strains with a vanishing component provide the most efficient actuation for the bending behaviors. This finding may explain the wide existence of anisotropic structures in plant tissues, such as the scale of pine cone [50] and the seed capsule of ice plant [14]. The microscale anisotropic structures in these plant tissues enable an anisotropic swelling in response to external humidity change, resulting in the maximum degrees of bending or unbending by absorbing the minimum amount of water in order to help spread their seeds easily. Thus, these anisotropic microstructures in plants could be an optimized result during their long-term natural evolution.

The PBs in phase diagrams are controlled by the different parameters m, n, p and q , where $q = L_1/L_2$ is the length ratio. It can be seen from Fig. 7a that the elastic moduli m of the two layers has little effect on the PBs, while the other three parameters n, p and q affect the variation of the PBs significantly. The variation of the thickness ratio causes a shrinkage of the bistable region and shifts the bifurcation point to higher values. On the other hand, increasing p gives rise to the enlargement of the bistable region, and shifts the bifurcation point to lower active strain. Such change in the bifurcation point is consistent with theoretical results reported in literature [8], where the bifurcation curvature or the bifurcation surface stress is inversely proportional to p^2 . Similar results on the bifurcation point can also be found in [39]. In addition, it is noted that the PBs for different m, n , and p shown in Fig. 7a–c are symmetric with respect to the line $\alpha_1 = \alpha_2$, while the PBs for $q = 1.25$ and 1.33 are not in a symmetric shape due to the loss of the symmetry of the bilayer. The bistable region shrinks when q increases, indicating that the larger the length-to-width ratio of the bilayer, the more difficult it is to transit into a bistable state. From the phase diagram discussed above, we can easily find the shortest active-strain route from a specific phase point to achieve the snap-through as discussed before. It should be noted that this current model is not accurate for extremely large active strains or significant change of mechanical properties involved, which is out of the scope of this work and will be studied in the future.

5. Conclusions

In this work, we have studied the bending behaviors of soft active bilayer structures with focus on their phase transition from bistability to monostability and their optimal actuation. The traditional Timoshenko's solution for the 2D bilayer beam has been modified to include the nonlinear effect of axial stretch on bending curvature. The FE results based on the Riks method have shown a good agreement with the theoretical solutions. The snap-through phenomena generated by anisotropic active strains are investigated based on the curvature and energy landscape from numerical simulations. We have also summarized the strain route to achieve the shape jump from a specific initial state. The phase diagrams for different geometrical parameters and material properties are presented for potential applications. It is found that anisotropic active strains can generate the optimal bending of bilayer plates. The theoretical model and phase diagram presented in this work will provide a guidance for future design of high-performance bilayer-based actuators and machines.

Acknowledgments

This work is supported by the USDA National Institute of Food and Agriculture, Hatch Project (USA) (No. 1016788) and the start-up fund from Michigan State University, USA. Y.L. acknowledges the partial support from the National Natural Science Foundation of China (11702198). C.C. thanks Prof. David Bigoni from the University of Trento, Italy for helpful discussion and comment.

References

- [1] J.-H. Na, et al., Programming reversibly self-folding origami with micropatterned photo-crosslinkable polymer trilayers, *Adv. Mater.* 27 (1) (2015) 79–85.
- [2] L.T. de Haan, et al., Humidity-responsive liquid crystalline polymer actuators with an asymmetry in the molecular trigger that bend, fold, and curl, *J. Am. Chem. Soc.* 136 (30) (2014) 10585–10588.
- [3] L. Ionov, Hydrogel-based actuators: possibilities and limitations, *Mater. Today* 17 (10) (2014) 494–503.
- [4] T. van Manen, S. Janbaz, A.A. Zadpoor, Programming the shape-shifting of flat soft matter, *Mater. Today* 21 (2) (2018) 144–163.
- [5] R.M. Erb, et al., Self-shaping composites with programmable bioinspired microstructures, *Nature Commun.* 4 (2013) 1712.
- [6] G. Gao, et al., Snap-buckling motivated controllable jumping of thermo-responsive hydrogel bilayers, *ACS Appl. Mater. Interfaces* 10 (48) (2018) 41724–41731.
- [7] X. Feng, Y. Huang, A.J. Rosakis, Multi-layer thin films/substrate system subjected to non-uniform misfit strains, *Int. J. Solids Struct.* 45 (13) (2008) 3688–3698.
- [8] N.J. Salamon, C.B. Masters, Bifurcation in isotropic thinfilm/substrate plates, *Int. J. Solids Struct.* 32 (3) (1995) 473–481.
- [9] E.K. Rodriguez, A. Hoger, A.D. McCulloch, Stress-dependent finite growth in soft elastic tissues, *J. Biomech.* 27 (4) (1994) 455–467.
- [10] L.B. Freund, Substrate curvature due to thin film mismatch strain in the nonlinear deformation range, *J. Mech. Phys. Solids* 48 (6) (2000) 1159–1174.
- [11] C. Cao, et al., Harnessing localized ridges for high-aspect-ratio hierarchical patterns with dynamic tunability and multifunctionality, *Adv. Mater.* 26 (11) (2014) 1763–1770.
- [12] C. Cao, et al., Tunable lotus-leaf and rose-petal effects via graphene paper origami, *Extreme Mech. Lett.* 4 (2015) 18–25.
- [13] J. Zang, et al., Stretchable and high-performance supercapacitors with crumpled graphene papers, *Sci. Rep.* 4 (2014) 6492.
- [14] M.J. Harrington, et al., Origami-like unfolding of hydro-actuated ice plant seed capsules, *Nature Commun.* 2 (2011) 337.
- [15] J.M. Boothby, T.H. Ware, Shape-switching bilayers enabled by liquid crystal elastomers, *Soft Matter* 13 (24) (2017) 4349–4356.
- [16] A. Agrawal, et al., Shape-responsive liquid crystal elastomer bilayers, *Soft Matter* 10 (9) (2014) 1411–1415.
- [17] J. Zhang, et al., Temperature-sensitive bending of bigel strip bonded by macroscopic molecular recognition, *Soft Matter* 8 (21) (2012) 5750–5752.
- [18] G. Stoychev, et al., Hole-programmed superfast multistep folding of hydrogel bilayers, *Adv. Funct. Mater.* 26 (42) (2016) 7733–7739.

- [19] J. Cui, J.G.M. Adams, Y. Zhu, Controlled bending and folding of a bilayer structure consisting of a thin stiff film and a heat shrinkable polymer sheet, *Smart Mater. Struct.* 27 (5) (2018) 055009.
- [20] Rees, E. Vouga, L. Mahadevan, Growth patterns for shape-shifting elastic bilayers, *Proc. Natl. Acad. Sci.* 114 (44) (2017) 11597–11602.
- [21] S. Timoshenko, Analysis of bi-metal thermostats, *J. Opt. Soc. Amer.* 11 (3) (1925) 233–255.
- [22] G.G. Stoney, The tension of metallic films deposited by electrolysis, *Proc. R. Soc. Lond. Ser. A Math. Phys. Eng. Sci.* 82 (553) (1909) 172–175.
- [23] L.B. Freund, S. Suresh, *Thin Film Materials: Stress, Defect Formation and Surface Evolution*, Cambridge University Press, 2004.
- [24] X. Feng, Y. Huang, A.J. Rosakis, On the stoney formula for a thin film/substrate system with nonuniform substrate thickness, *J. Appl. Mech.* 74 (6) (2007) 1276–1281.
- [25] J. Zang, F. Liu, Modified Timoshenko formula for bending of ultrathin strained bilayer films, *Appl. Phys. Lett.* 92 (2) (2008) 021905.
- [26] L.B. Freund, J.A. Floro, E. Chason, Extensions of the stoney formula for substrate curvature to configurations with thin substrates or large deformations, *Appl. Phys. Lett.* 74 (14) (1999) 1987–1989.
- [27] Noè A. Caruso, et al., Spontaneous morphing of equibiaxially pre-stretched elastic bilayers: The role of sample geometry, *Int. J. Mech. Sci.* 149 (2018) 481–486.
- [28] M.W. Hyer, The room-temperature shapes of four-layer unsymmetric cross-ply laminates, *J. Compos. Mater.* 16 (4) (1982) 318–340.
- [29] C.B. Masters, N.J. Salamon, Geometrically nonlinear stress-deflection relations for thin film/substrate systems, *Internat. J. Engrg. Sci.* 31 (6) (1993) 915–925.
- [30] C.B. Masters, N.J. Salamon, Geometrically nonlinear stress-deflection relations for thin film/substrate systems with a finite element comparison, *J. Appl. Mech.* 61 (4) (1994) 872.
- [31] S. Alben, B. Balakrishnan, E. Smela, Edge effects determine the direction of bilayer bending, *Nano Lett.* 11 (6) (2011) 2280–2285.
- [32] A.M. Abdullah, P.V. Braun, K.J. Hsia, Bifurcation of self-folded polygonal bilayers, *Appl. Phys. Lett.* 111 (10) (2017) 104101.
- [33] M. Pezzulla, et al., Geometry and mechanics of thin growing bilayers, *Soft Matter* 12 (19) (2016) 4435–4442.
- [34] M. Finot, S. Suresh, Small and large deformation of thick and thin-film multi-layers: Effects of layer geometry, plasticity and compositional gradients, *J. Mech. Phys. Solids* 44 (5) (1996) 683–721.
- [35] S. Armon, et al., Geometry and mechanics in the opening of chiral seed pods, *Science* 333 (6050) (2011) 1726–1730.
- [36] E. Efrati, E. Sharon, R. Kupferman, Elastic theory of unconstrained non-Euclidean plates, *J. Mech. Phys. Solids* 57 (4) (2009) 762–775.
- [37] D.P. Holmes, A.J. Crosby, Snapping surfaces, *Adv. Mater.* 19 (21) (2007) 3589–3593.
- [38] Q. Zhao, et al., A bioinspired reversible snapping hydrogel assembly, *Mater. Horiz.* 3 (5) (2016) 422–428.
- [39] Z. Chen, et al., Nonlinear geometric effects in mechanical bistable morphing structures, *Phys. Rev. Lett.* 109 (11) (2012).
- [40] Y. Liu, et al., Anisotropic swelling in fiber-reinforced hydrogels: An incremental finite element method and its applications in design of bilayer structures, *Int. J. Appl. Electromagn. Mech.* 08 (07) (2016) 1640003.
- [41] P. Nardinocchi, M. Pezzulla, L. Teresi, Anisotropic swelling of thin gel sheets, *Soft Matter* 11 (8) (2015) 1492–1499.
- [42] A.I. Egunov, J.G. Korvink, V.A. Luchnikov, Polydimethylsiloxane bilayer films with an embedded spontaneous curvature, *Soft Matter* (2015).
- [43] J. Kim, et al., Reversible self-bending soft hydrogel microstructures with mechanically optimized designs, *Chem. Eng. J.* 321 (2017) 384–393.
- [44] Z. Chen, et al., 2011, Tunable helical ribbons, *Appl. Phys. Lett.* 98 (1) (2011) 011906.
- [45] E. Abbena, S. Salamon, A. Gray, *Modern Differential Geometry of Curves and Surfaces with Mathematica*, Chapman and Hall/CRC, 2017.
- [46] Z.P. Bažant, L. Cedolin, *Stability of Structures: Elastic, Inelastic, Fracture and Damage Theories*, WORLD SCIENTIFIC, 2010.
- [47] Y. Liu, et al., A robust riks-like path following method for strain-actuated snap-through phenomena in soft solids, *Comput. Methods Appl. Mech. Engrg.* 323 (2017) 416–438.
- [48] E. Riks, An incremental approach to the solution of snapping and buckling problems, *Int. J. Solids Struct.* 15 (7) (1979) 529–551.
- [49] M. Finot, et al., Large deformation and geometric instability of substrates with thin-film deposits, *J. Appl. Phys.* 81 (8) (1997) 3457–3464.
- [50] C. Dawson, J.F.V. Vincent, A.-M. Rocca, How pine cones open, *Nature* 390 (6661) (1997) 668–668.